Supplemental Material

High-harmonic generation in semi-Dirac and Weyl semimetals with broken time-reversal symmetry: Exploration of the merging of Weyl nodes

Luka Medic,* Jernej Mravlje, Anton Ramšak, and Tomaž Rejec Jožef Stefan Institute, Jamova 39, SI-1000 Ljubljana, Slovenia and Faculty of Mathematics and Physics, University of Ljubljana, Jadranska 19, SI-1000 Ljubljana, Slovenia

S1. Weyl and semi-Dirac regimes

To determine the nodes of the model Hamiltonian described in the main text we search for solutions of $\epsilon_{c,v}=0$, or equivalently $d_x=d_y=d_z=0$. From $d_y=d_z=0$, we observe that bk_y and ck_z should take values 0 or π . Considering the constraint $d_x=0$, we obtain $|\cos(ak_x)|=|(\gamma \mp t_y \mp t_z)/t_x| \le 1$, where the upper and lower signs correspond to $bk_y, ck_z=0$ and π , respectively. The nodes thus occur for values of γ that obey $-t_x \pm t_y \pm t_z \le \gamma \le t_x \pm t_y \pm t_z$. For values of γ in the interior of that interval one finds pairs of Weyl-nodes, whereas at extremal points $(\gamma = \pm t_x \pm t_y \pm t_z)$ the Weyl-nodes merge resulting in semi-Dirac points (8 total). These semi-Dirac points are located at time-reversal invariant momenta (TRIM). This is illustrated in Fig. S1, where the regions of higher excitation densities N_c indicate the positions of Weyl and semi-Dirac nodes in the Brillouin zone (BZ).

Let us examine the low-energy spectrum. We denote the positions of the four pairs of Weyl nodes as $\pm \mathbf{k}_0^{(\pm,\pm)}$, where the + and - signs in the superscript correspond to $bk_y, ck_z = 0$ and π , respectively. The nodes are separated in the k_x direction. Let $2k_0^{(\pm,\pm)}$ (or $2k_0$ for brevity) denote the distance between them. We expand energy $\epsilon^{(\pm,\pm)}(\mathbf{q}) \equiv \epsilon(\mathbf{k}_0^{(\pm,\pm)} + \mathbf{q})$ up to the second order in the displacement vector \mathbf{q} :

$$\epsilon^{(\pm,\pm)}(\mathbf{q}) \approx \sqrt{\left(\frac{(v_x q_x)^2}{2t_x}\cos(ak_0) + v_x q_x \sin(ak_0)\right)^2 + (v_y q_y)^2 + (v_z q_z)^2}$$
(S1.1)

where we introduced $v_x = at_x$, $v_y = bt_y$, and $v_z = ct_z$. For $\sin(ak_0) = 0$, we have a semi-Dirac point at $k_x = 0$ or π/a with a parabolic (q_x^2) and 2D conical (in the q_y-q_z plane) dispersion. For $\sin(ak_0) \neq 0$, we have a pair of Weyl nodes at $k_x = \pm k_0$ with, in general, anisotropic linear dispersion that depends on k_0 .

The above derivation simplifies in the specific case we present in the paper, where a=b=c=1 and $t_x=t_y=t_z=1$. In this case, we identify five qualitatively different regimes:

- $|\gamma| > 3$: This regime corresponds to a gapped insulator phase, similar to the one presumably observed in the ZrTe₅.
- $|\gamma| = 3$: In this regime, we have a semi-DSM with a single semi-Dirac node. For $\gamma = 3$ it is at $\mathbf{k}_0 = (0, 0, 0)$ and for $\gamma = -3$ it is at $\mathbf{k}_0 = (\pi, \pi, \pi)$.
- $1 < |\gamma| < 3$: Within this regime, we encounter WSMs with one pair of Weyl nodes; for $1 < \gamma < 3$ they are at $\mathbf{k}_0 = (\pm \arccos(\gamma 2), 0, 0)$ and for $-3 < \gamma < -1$ they are at $\mathbf{k}_0 = (\pm \arccos(\gamma + 2), \pi, \pi)$
- $|\gamma| = 1$: This regime represents a semi-DSM with three semi-Dirac nodes. For $\gamma = 1$ they are at $\mathbf{k}_0 = (\pi, 0, 0), (0, \pi, 0)$ and $(0, 0, \pi)$, while for $\gamma = -1$ they are at $\mathbf{k}_0 = (0, \pi, \pi), (\pi, 0, \pi)$ and $(\pi, \pi, 0)$.
- $|\gamma| < 1$: This regime corresponds to a WSM featuring two pairs of Weyl nodes which are at $\mathbf{k}_0 = (\pm \arccos(\gamma), \pi, 0)$ and $(\pm \arccos(\gamma), 0, \pi)$.

Conical dispersion around the Weyl nodes becomes isotropic when $k_0 = \pi/2$ ($\gamma = \pm 2$). In Fig. S2, an additional chart, accompanying Fig. 2 of the main text, illustrates the energy spectra along high symmetry lines.

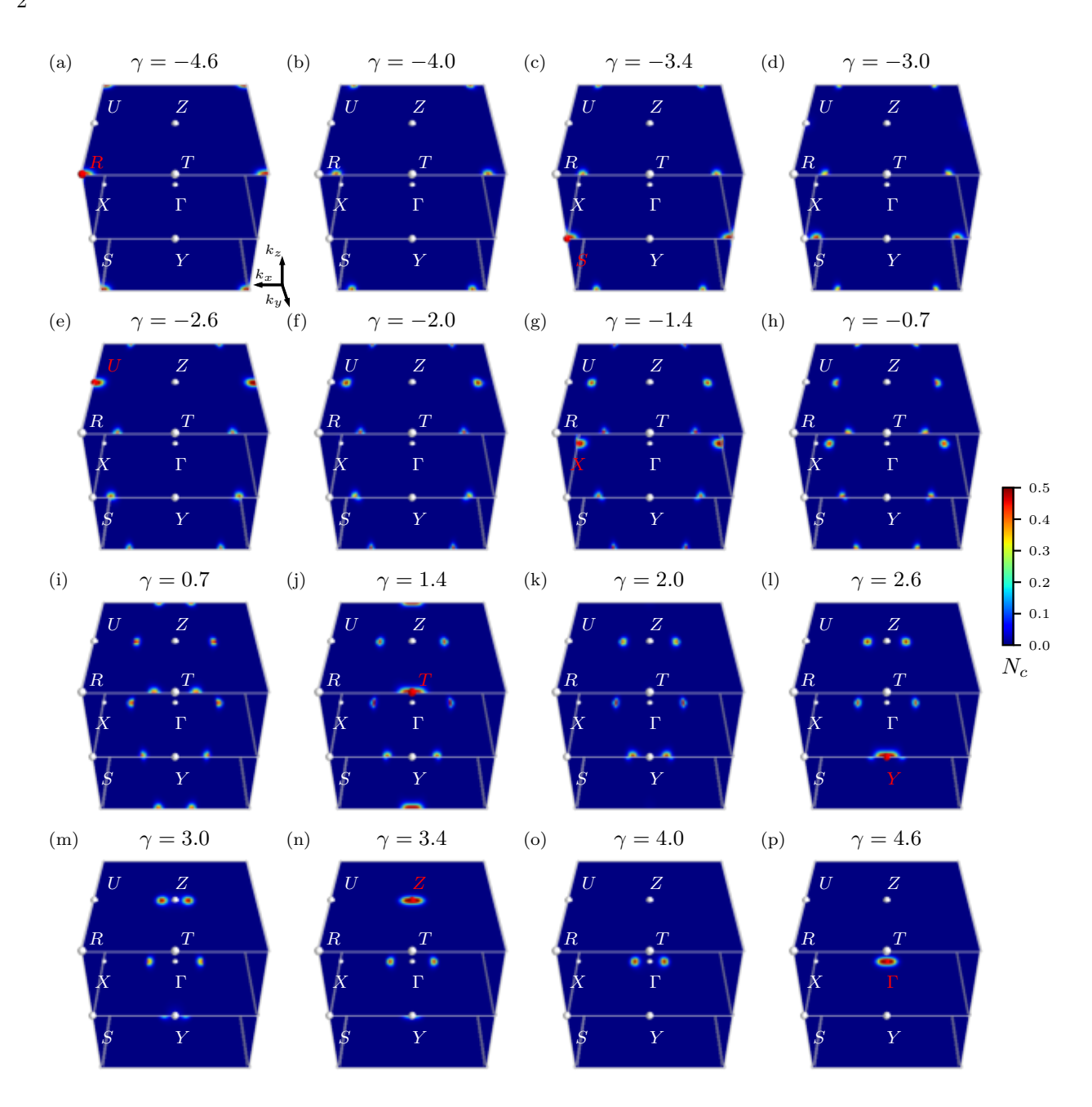


Figure S1. Excitations N_c in the BZ of a primitive orthorhombic lattice with lattice constants a=b=c=1 and hopping parameters $t_x=3$, $t_y=1$, and $t_z=0.6$. Semi-Dirac points (8 in total) are highlighted with red labels (a,c,e,g,j,l,n,p).

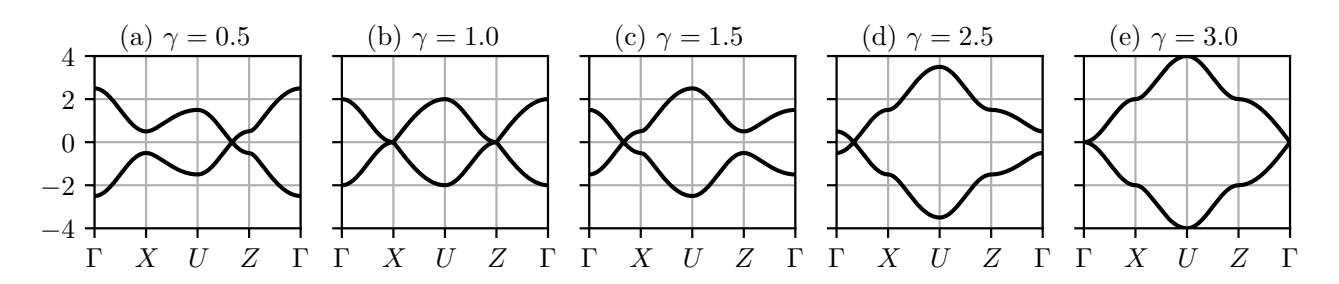


Figure S2. Energy spectra along high symmetry lines for various values of γ . The parabolic-2D-conical dispersion is observed in (b) at X and Z, and in (e) at Γ .

S2. Derivation of symmetry relation $\mathcal{I}(\gamma) = \mathcal{I}(-\gamma)$

In this section we will use the notation $\tilde{\mathbf{v}} = (v_x, -v_y, v_z)$ where \mathbf{v} is an arbitrary 3D vector. From the symmetry relation stated in Eq. (1) of the main text, we obtain the following relationships:

$$\omega_{mn}(\mathbf{k}, -\gamma) = \omega_{mn}(\mathbf{R} - \tilde{\mathbf{k}}, \gamma) \tag{S2.1}$$

$$\mathbf{d}_{mn}(\mathbf{k}, -\gamma) = -\tilde{\mathbf{d}}_{mn}(\mathbf{R} - \tilde{\mathbf{k}}, \gamma)e^{i\varphi_{mn}}$$
(S2.2)

$$\mathbf{p}_{mn}(\mathbf{k}, -\gamma) = -\tilde{\mathbf{p}}_{mn}(\mathbf{R} - \tilde{\mathbf{k}}, \gamma)e^{i\varphi_{mn}}$$
(S2.3)

where the factor $e^{i\varphi_{mn}}$ represents an arbitrary gauge factor.

By inserting identities (S2.1)-(S2.3) into the SBE [i.e., Eq. (2) of the main text], we obtain:

$$\rho_{mn}^{\mathbf{k}}(t, -\gamma, \mathbf{E}) = \rho_{mn}^{\mathbf{R} - \tilde{\mathbf{k}}}(t, \gamma, -\tilde{\mathbf{E}})e^{-i\varphi_{mn}}.$$
 (S2.4)

Inserting the relations (S2.3) and (S2.4) into Eq. (3) of the main text, we obtain a relation for the total current:

$$\mathbf{J}\left(-\gamma, \mathbf{E}\right) = -\tilde{\mathbf{J}}\left(\gamma, -\tilde{\mathbf{E}}\right),\tag{S2.5}$$

which is gauge independent.

Additionally, by following similar steps as described above, we can establish that inversion symmetry leads to the reversal of the total current when the direction of the electric field is reversed, i.e. $\mathbf{E} \to -\mathbf{E}$ results in $\mathbf{J} \to -\mathbf{J}$.

Combining these two results, we obtain:

$$\mathbf{J}\left(-\gamma, \mathbf{E}\right) = \tilde{\mathbf{J}}\left(\gamma, \tilde{\mathbf{E}}\right). \tag{S2.6}$$

In the specific case presented in our paper, where the driving pulse has z polarization, we have $\mathcal{I}(\gamma) = \mathcal{I}(-\gamma)$, and $\mathcal{I}_y(\gamma = 0) = 0$.

S3. Dependence of response on ω_0 and E_0 ; BZ maps of contributions to the response

In Fig. S3 we show peak intensities of third anomalous harmonic as a function of γ for several pulse frequencies ω_0 and amplitudes of the electric field E_0 . For small ω_0 and E_0 one clearly sees response sharply peaking in the proximity of the two semi-Dirac regimes, $\gamma=1$ and $\gamma=3$. In the intermediate Weyl regimes, the response is suppressed, which is explained in terms of the cancelation of the response for each individual Weyl point as long as it can be considered well-separated. The localization of the response next to the Weyl points for small ω_0 and E_0 is illustrated in the insets that show the third harmonic contribution to anomalous current as a function of time and k_x .

When E_0 is increased, the total magnitude of the response is increased, correlating with the density of the excitations (up to the saturation point $N_c = 0.5$) and their extent in the BZ that both increase (see Fig. S4). The response increases also in the strict Weyl regime around $\gamma = 2$. This is rationalized by a weakening of the well-separatedness criterion as seen in the insets of Fig. S3 with contributions to the third harmonic between the two Weyl nodes that become more significant with increasing E_0 .

The dependence on ω_0 is more subtle. With progressively increasing ω_0 the magnitude of response in Fig. S3 drops and the γ dependence becomes significantly milder. We rationalize this by noting that as ω_0 increases, the resonant condition $\hbar\omega_{cv} = n\hbar\omega_0$ ($n \in \mathbb{N}$) [1] shifts further away from the nodes. The transition dipole moments \mathbf{d}_{vc} decrease there [2]. As a result, for large ω_0 , the density of excitations reduces near the Weyl nodes and increases somewhat away from them (see Fig. S4). Thus, with increasing ω_0 one is less sensitive to the low-energy details, and the response as a function of γ becomes more uniform. [We note that when changing ω_0 , we have also scaled all the other temporal scales $(T, \tau, \text{ and } T_2)$ such that the characteristics of the pulse remain unchanged.]

To illustrate how the response is distributed in the BZ, and to illustrate how localization of the response to the Weyl node is affected by ω_0 , we show maps of the time evolution of the third harmonic contribution to the current on Fig. S5 at $\gamma=2.1$. Because we found that the current is nearly odd when k_z is flipped $J_y(k_x,k_y,k_z) \simeq -J_y(k_x,k_y,-k_z)$, we show combined quantity $\Sigma_y(\mathbf{k}) = (J_y(k_x,k_y,k_z) + J_y(k_x,k_y,-k_z))/2$. These time evolutions are displayed as cross sections $(k_y-k_z, k_x-k_y, \text{ and } k_x-k_z)$, traversing near the Weyl node at $\mathbf{k}_0 = (1.47,0,0)$. Examining these results, we observe that the contributions to higher harmonics are

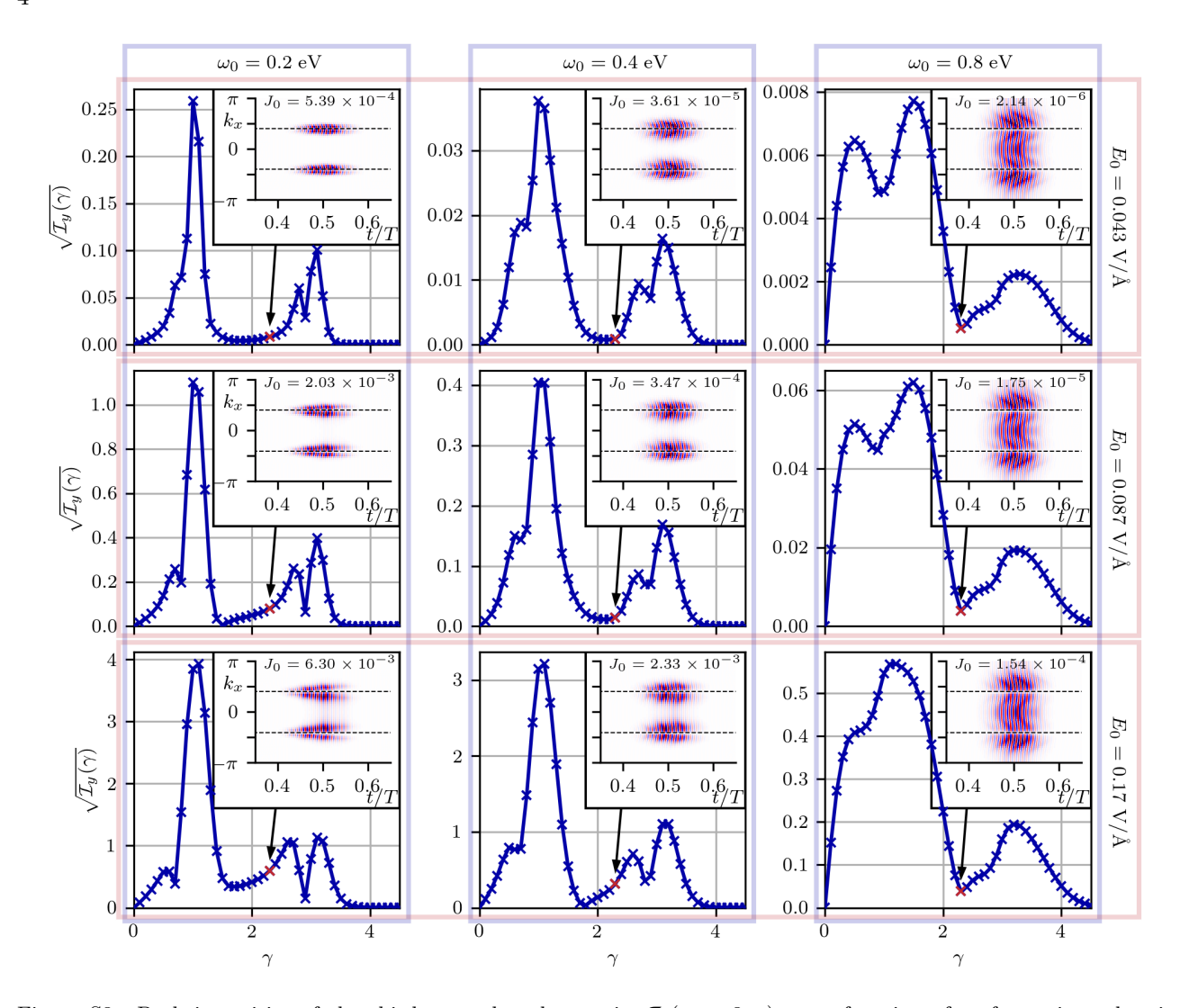


Figure S3. Peak intensities of the third anomalous harmonic, $\mathcal{I}_y(\omega=3\omega_0)$, as a function of γ , for various electric field carrier frequencies ω_0 (columns) and amplitudes E_0 (rows). *Inset:* Time series of sliced contributions to the third harmonic of the anomalous current $J_y^{3\omega_0}(t,k_x) = \sum_{k_y,k_z} J_y^{3\omega_0}(t,\mathbf{k})$. J_0 indicates the maximal amplitude of $J_y^{3\omega_0}(t,k_x)$ for a given ω_0 , E_0 , and $\gamma=2.3$. Dashed lines indicate the positions of Weyl nodes.

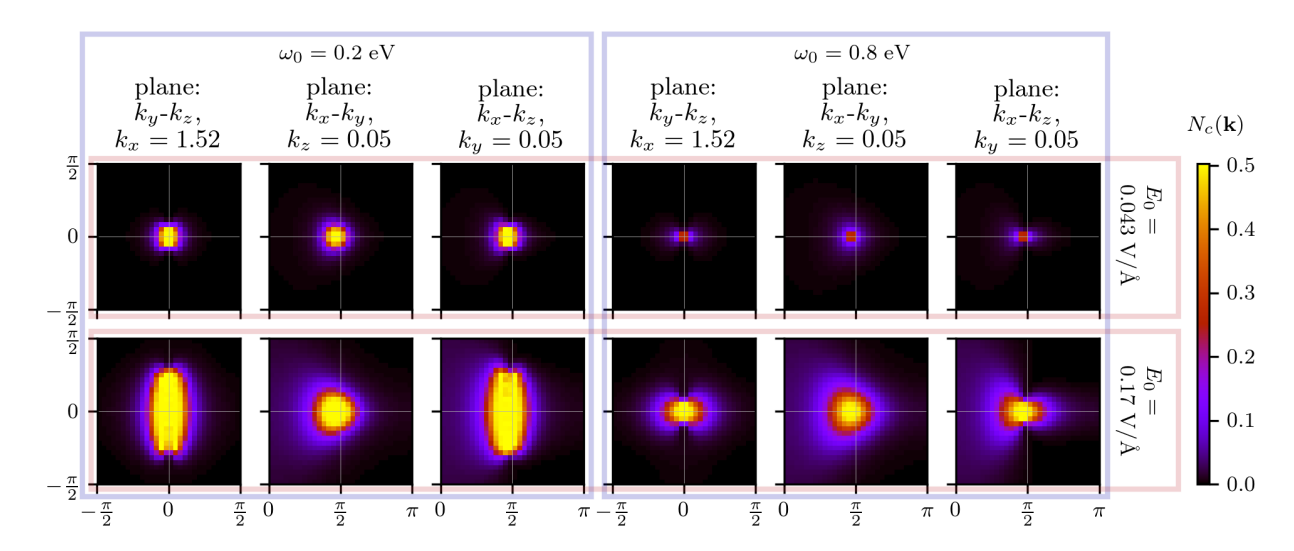


Figure S4. Excitations $N_c(\mathbf{k})$ at t = T/2 for two different values of ω_0 and E_0 . Excitations are presented as cross sections $(k_y-k_z, k_x-k_y, \text{ and } k_x-k_z)$, traversing near the Weyl node at $\mathbf{k}_0 = (1.47, 0, 0)$. The parameter γ is set to 2.1.

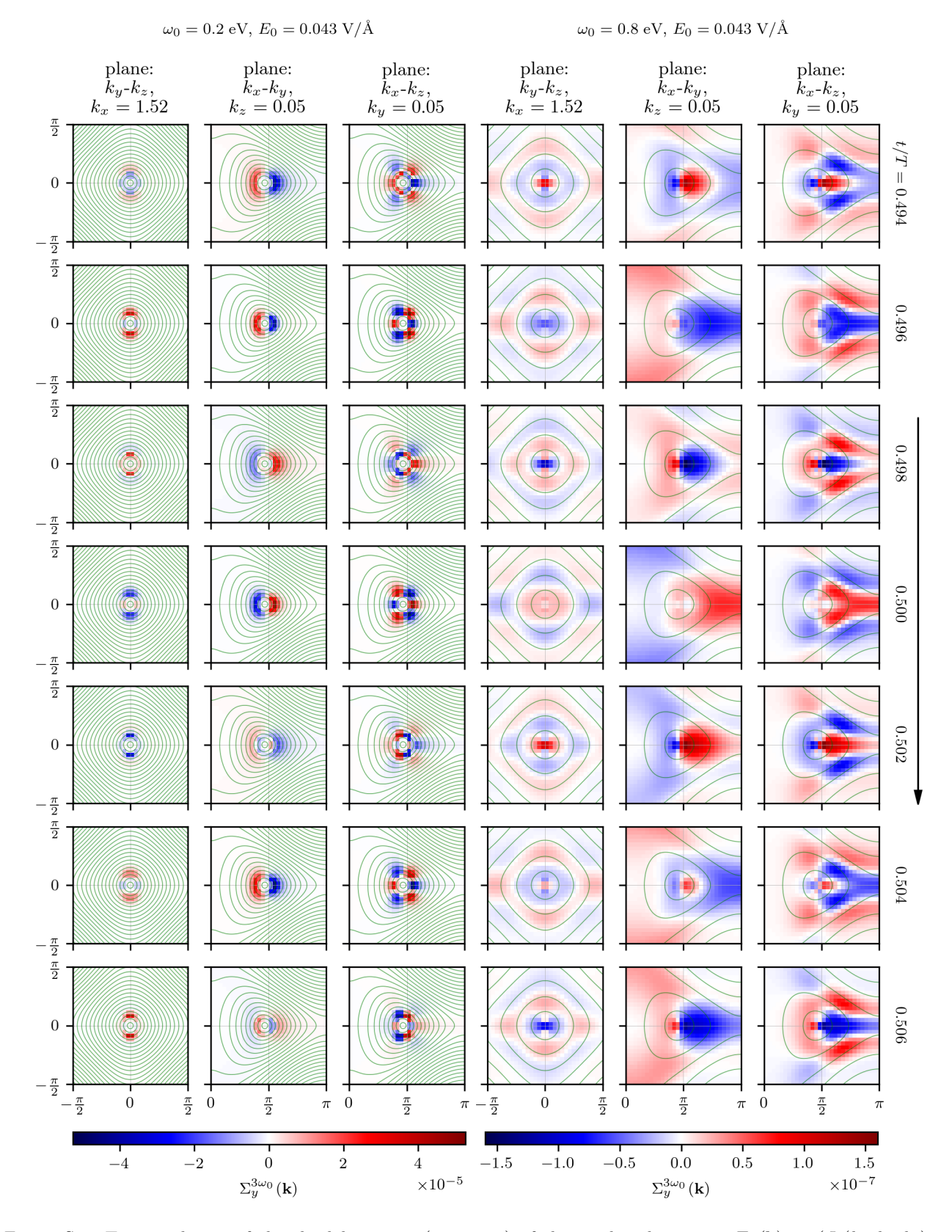


Figure S5. Time evolution of the third harmonic ($\omega=3\omega_0$) of the combined quantity $\Sigma_y(\mathbf{k})=(J_y(k_x,k_y,k_z)+J_y(k_x,k_y,-k_z))/2$. The contours indicate the resonant conditions $\hbar\omega_{cv}=n\hbar\omega_0$ for $n=1,2,3\ldots$

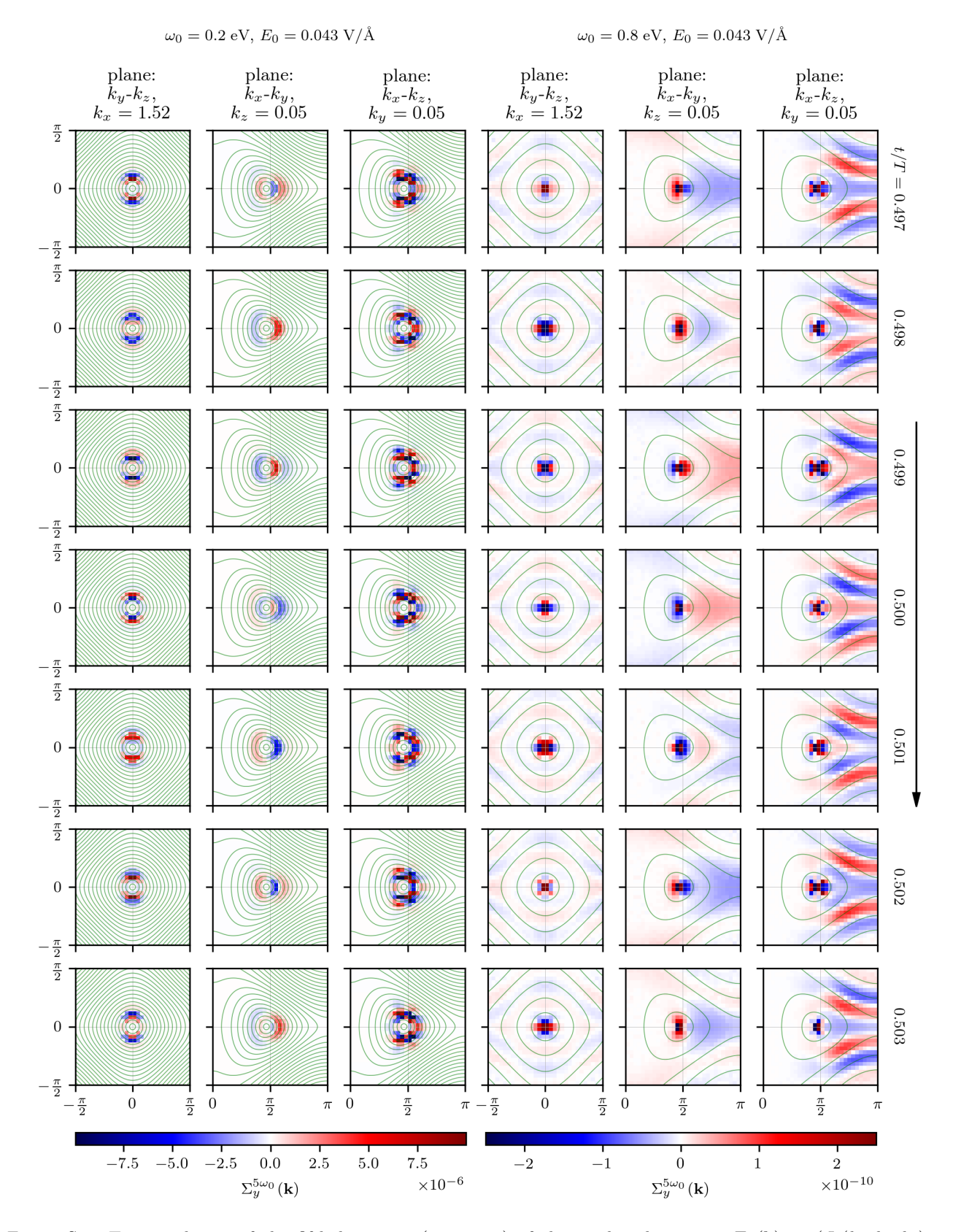


Figure S6. Time evolution of the fifth harmonic ($\omega=5\omega_0$) of the combined quantity $\Sigma_y(\mathbf{k})=(J_y(k_x,k_y,k_z)+J_y(k_x,k_y,-k_z))/2$. The contours indicate the resonant conditions $\hbar\omega_{cv}=n\hbar\omega_0$ for $n=1,2,3\ldots$

concentrated near the Weyl node in the well-separated regime ($\omega_0 = 0.2 \text{ eV}$). However, for $\omega_0 = 0.8 \text{ eV}$, these contributions are present even at **k** far from **k**₀, again indicating that the assumption of well-separated nodes does not apply for large ω_0 .

The observations on the localization of contributions, when ω_0 is small, can also be made for higher harmonics. The fifth harmonic is shown in Fig. S6. Although oscillations are faster compared to the third harmonic (note that the snapshots are taken at shorter time intervals as in Fig. S5). As expected, the frequencies of these oscillations are $\omega = m\omega_0$, where m denotes the harmonic order, specifically 3 and 5.

S4. C_{2z} rotational symmetry and vanishing anomalous current for a well-separated Weyl node

In this section, we investigate the behavior of a well-separated Weyl node characterized by linear dispersion in the low-energy limit, following the approach outlined in Ref. [2]. The Hamiltonian for an anisotropic Weyl cone is given by $H(\mathbf{q}) = \sum_i v_i q_i \sigma_i$, where v_i are the Fermi velocities, $\mathbf{q} = (q_x, q_y, q_z)^T$ is the displacement vector from the Weyl node, and σ_i are Pauli matrices. Suppose we apply an electric field in the z direction. In this case, the Hamiltonian preserves the C_{2z} rotational symmetry in the q_x - q_y plane, given by:

$$\sigma_z H(\mathbf{q}(t))\sigma_z = H(\mathbf{q}'(t)),$$
 (S4.1)

where we use the notation $\mathbf{q}(t) = \mathbf{q} + \mathbf{A}(t)$, $\mathbf{q}'(t) = \mathbf{q}' + \mathbf{A}(t)$, and $\mathbf{q}' = (-q_x, -q_y, q_z)$.

Now let us derive the anomalous current produced by a well-separated node. Using the notation $N_{c/v} = \rho_{cc/vv}$ and $P = \rho_{vc} = \rho_{cv}^*$ (omitting superscripts **q** for brevity), we rewrite the SBE, Eq. (2) of the main text, as:

$$\partial_t N_c(t) = -\partial_t N_v(t) = 2\mathbf{E}(t) \cdot \mathfrak{Im}\{\mathbf{d}_{cv} P(t)\}$$
(S4.2)

$$\partial_t P(t) = \left[i\omega_{cv} - 1/T_2 + i\mathbf{E}(t) \cdot (\mathbf{d}_{cc} - \mathbf{d}_{vv}) \right] P(t) + i\mathbf{E}(t) \cdot \mathbf{d}_{cv}^* \left(1 - 2N_c(t) \right).$$
 (S4.3)

For z polarization of the electric field, we have $(\mathbf{d}_{cc} - \mathbf{d}_{vv})_z = 0$ (see Ref. [2]). Now, let us consider the transformation $\mathbf{q} \to \mathbf{q}'$ which leads to transformations:

$$E_z \to E_z$$
 (S4.4)

$$\omega_{mn} \to \omega_{mn}$$
 (S4.5)

$$(\mathbf{d}_{cv})_y \to (\mathbf{d}_{cv})_y$$
 (S4.6)

$$(\mathbf{d}_{cv})_z \to -(\mathbf{d}_{cv})_z. \tag{S4.7}$$

Combining this with the initial conditions $N_v(0) = 1$, $N_c(0) = P(0) = 0$, we conclude that the density matrix elements transform as $N_{c/v} \to N_{c/v}$ and $P \to -P$.

Next, we rewrite the contributions to the anomalous current $J_{\nu}(\mathbf{q})$ as:

$$J_y(\mathbf{q}) = -\sum_m (\mathbf{V}_m)_y N_m + 2\omega_{cv} \mathfrak{Im}\{(\mathbf{d}_{cv})_y P\}$$
 (S4.8)

where $\mathbf{V}_c = -\mathbf{V}_v = \mathbf{p}_{cc} = \nabla_{\mathbf{q}} \epsilon_c = \mathbf{q}/\epsilon_c$ is evaluated near the Weyl node, where the dispersion is linear. The y component of \mathbf{V}_c transforms as $(\mathbf{V}_c)_y \to -(\mathbf{V}_c)_y$. Together with Eq. (S4.6) and the transformations for $N_{c/v}$ and P, we find $J_y(\mathbf{q}) = -J_y(\mathbf{q}')$. This implies that the contributions to the total anomalous current cancel in pairs for each well-separated Weyl node:

$$J_{y} = \sum_{\mathbf{q}} J_{y}(\mathbf{q}) = \frac{1}{2} \left(\sum_{\mathbf{q}} J_{y}(\mathbf{q}) + \sum_{\mathbf{q}'} J_{y}(\mathbf{q}') \right)$$
$$= \frac{1}{2} \sum_{\mathbf{q}} \left(J_{y}(\mathbf{q}) + J_{y}(\mathbf{q}') \right) = 0. \tag{S4.9}$$

S5. Tilted cones in WSM

In this section, we introduce an additional term in the Hamiltonian to describe the tilt of the Weyl cones. The modified Hamiltonian, denoted as $H'(\mathbf{k})$, is given by

$$H'(\mathbf{k}) = d_0(\mathbf{k})I + H(\mathbf{k}), \tag{S5.1}$$

where $H(\mathbf{k})$ is the original Hamiltonian, and I is the 2×2 identity matrix. The function $d_0(\mathbf{k})$ represents an arbitrary periodic function of the crystal momentum \mathbf{k} . We choose this function in a way that it tilts the Weyl cones while maintaining the occupancy of the energy bands unchanged, resulting in a tilted type-I Weyl semimetal. A specific example of such a function is $d_0 = \delta(\cos(k_x) - \gamma)$, where δ is a parameter that quantifies the tilt along the k_x direction.

The introduction of $d_0(\mathbf{k})$ causes a shift in the energy spectrum, given by $\epsilon'_{c,v}(\mathbf{k}) = d_0(\mathbf{k}) + \epsilon_{c,v}(\mathbf{k})$. However, despite this modification, the corresponding wavefunctions remain unchanged: $|n, \mathbf{k}\rangle' = |n, \mathbf{k}\rangle$. Additionally, the transition frequencies and transition dipole moments are also unaffected, namely $\omega'^{\mathbf{k}}_{mn} = \omega^{\mathbf{k}}_{mn}$ and $\mathbf{d}'^{\mathbf{k}}_{mn} = \mathbf{d}^{\mathbf{k}}_{mn}$. Furthermore, the off-diagonal elements $(m \neq n)$ of the group-velocity matrix are also unaffected:

$$\mathbf{p}_{mn}^{\prime \mathbf{k}} = i\mathbf{d}_{mn}^{\prime \mathbf{k}} \omega_{mn}^{\prime \mathbf{k}} = i\mathbf{d}_{mn}^{\mathbf{k}} \omega_{mn}^{\mathbf{k}} = \mathbf{p}_{mn}^{\mathbf{k}}, \tag{S5.2}$$

however, the diagonal elements (m = n) change as follows:

$$\mathbf{p}_{mm}^{\prime \mathbf{k}} = \mathbf{V}_{m}^{\prime \mathbf{k}} = \nabla_{\mathbf{k}} \epsilon_{m}^{\prime \mathbf{k}} = \nabla_{\mathbf{k}} (d_{0}^{\mathbf{k}} + \epsilon_{m}^{\mathbf{k}}) = \nabla_{\mathbf{k}} d_{0}^{\mathbf{k}} + \mathbf{V}_{m}^{\mathbf{k}}. \tag{S5.3}$$

When considering the time evolution of the density matrix (Eq. (2) of the main text) under the influence of the tilted Hamiltonian $H'(\mathbf{k})$, we find that if the initial conditions satisfy $\rho_{mn}^{\prime\mathbf{k}}(t=0) = \rho_{mn}^{\mathbf{k}}(t=0)$, which is true in the type-I Weyl semimetal, then the density matrix at any time t remains the same for both the original and tilted Hamiltonians, $\rho_{mn}^{\prime\mathbf{k}}(t) = \rho_{mn}^{\mathbf{k}}(t)$.

Next, we consider the current density $\mathbf{J}'(t)$. By substituting the expressions (S5.2) and (S5.3) into the Eq. (3), we obtain the current density under the tilt as:

$$\mathbf{J}'(t) = -\sum_{\mathbf{k}} \left[\sum_{m} (\mathbf{V}_{m}^{\prime \mathbf{k}(t)} \rho_{mm}^{\prime \mathbf{k}}(t)) + \sum_{m \neq n} (\mathbf{p}_{nm}^{\prime \mathbf{k}(t)} \rho_{mn}^{\prime \mathbf{k}}(t)) \right] = \mathbf{J}(t) - \sum_{\mathbf{k}} \left[\sum_{m} \nabla_{\mathbf{k}(t)} d_{0}^{\mathbf{k}(t)} \rho_{mm}^{\mathbf{k}}(t) \right]$$

$$\stackrel{\text{(a)}}{=} \mathbf{J}(t) - \sum_{\mathbf{k}} \nabla_{\mathbf{k}} d_{0}^{\mathbf{k}} \to \mathbf{J}(t) - \int_{\mathrm{BZ}} \nabla_{\mathbf{k}} d_{0}^{\mathbf{k}} \, \mathrm{d}V_{\mathbf{k}} \stackrel{\text{(b)}}{=} \mathbf{J}(t) - \int_{\partial \mathrm{BZ}} d_{0}^{\mathbf{k}} \, \mathrm{d}\mathbf{S}_{\mathbf{k}} \stackrel{\text{(c)}}{=} \mathbf{J}(t). \tag{S5.4}$$

In the above derivation, BZ denotes the Brillouin zone, and ∂ BZ represents its boundary. Several relations have been employed in this process, including: (a) $\sum_{m} \rho_{mm}^{\mathbf{k}} = 1$, (b) the Gauss theorem, and (c) the periodicity of $d_0^{\mathbf{k}}$. Equation (S5.4) illustrates that the tilt induced by d_0 does not alter the total current.

Note that the above argumentation relies on a single occupancy at every momentum point. However, this condition does not apply to over-tilted, type-II WSMs that exhibit hyperboloidal electron and hole pockets [3] where the occupancy is double or zero, respectively. We leave further investigation of type-II WSMs for future studies.

S6. Decoupled left- and right-handed Weyl spinors

The linearized regime of well-separated Weyl nodes discussed in the main text is analogous to the model outlined in Ref. [2]. In this reference, the authors explicitly treat two decoupled Hamiltonians, each corresponding to a distinct, left and right, chirality of the Weyl spinor. As mentioned in the main text, our findings differ from those reported in Ref. [2], specifically regarding the anomalous higher-order responses. The objective of this section is to clarify this matter.

It is crucial to note that the finite nature of the first harmonic stems from topologically non-trivial 2D slices, characterized by a non-zero Chern number, located between the Weyl nodes. Following Ref. [2], this corresponds to the fourth term in Eq. (22) which, upon integration, yields a linear response. However, the remaining terms in Eq. (22) of Ref. [2] are multiplied by either N_c (excitations) or P (interband polarization), which invalidates the application of the same topological argument used for the first harmonic also to the higher ones.

To illustrate the different behavior between the first and higher harmonics in numerics, we reproduced the analysis presented in Fig. 3 of Ref. [2]. Our results are displayed in Fig. S7, illustrating the anomalous harmonics using three different integration region cut-offs, α_{cut} . The selected cut-offs offer evidence that higher harmonics diminish as α_{cut} is increased, whereas the first harmonic remains unchanged.

In the analytical treatment presented in Ref. [2], one has to carefully evaluate Eq. (23) (the fifth term of Eq. (22)), specifically when approximating $N_c(\mathbf{k}_0, t)$. Despite the cancellation around Weyl nodes (as indicated by the sgn function in Eq. (24) of Ref. [2]), the substitution of $N_c(\mathbf{k}_0, t)$ with $N_c(\mathbf{k}_{0w}, t)$ renders contributions far from the Weyl nodes as finite, while excitations actually vanish there (as depicted in Fig. 1 of Ref. [2]).

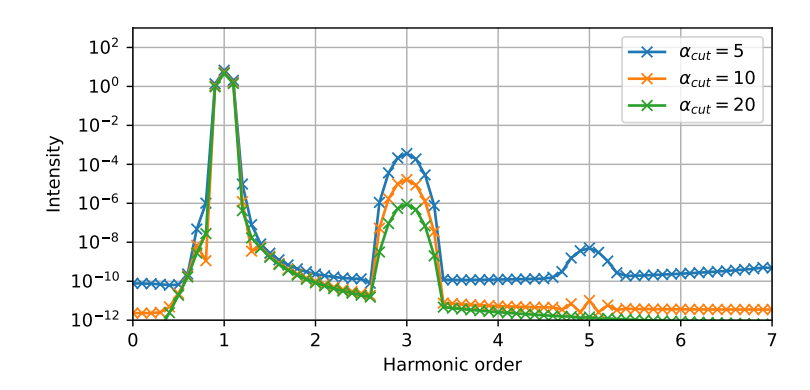


Figure S7. Results for the parameters of Ref. [2] for various cut-off values α_{cut} .

To resolve these issues, it is crucial to establish the rotational symmetry with respect to each isolated Weyl node, Eq. (6) of the main text, where contributions to anomalous higher-order harmonics cancel out in pairs. Specifically, this reduces the relevant integration interval in Eq. (24) of Ref. [2] to $(\Lambda - 2b, \Lambda)$:

$$j_y(t) = \frac{2E_z(t)}{(2\pi)^3} \int d^3 \mathbf{k}_0 \frac{(k_{0x} + b) N_c(\mathbf{k}_0, t)}{\left[(k_{0x} + b)^2 + k_{0y}^2 + k_{0z}^2 \right]^{3/2}}$$
 (S6.1)

$$= \frac{2E_z(t)}{(2\pi)^2} \int_{\Lambda-2b}^{\Lambda} dk_{0x} \int_0^{\infty} k_{\perp} dk_{\perp} \frac{(k_{0x} + b) N_c(\mathbf{k}_0, t)}{\left[k_{\perp}^2 + (k_{0x} + b)^2\right]^{3/2}}.$$
 (S6.2)

Further, evaluating the upper bound of j_y by using the substitution $N_c(\mathbf{k}_0, t) \to N_c^{\max}(t)$, where $N_c^{\max}(t) = \max_{k_{0x} \in (\Lambda - 2b, \Lambda)} [N_c(\mathbf{k}_0, t)]$, we get

$$j_y(t) \le \frac{2E_z(t)}{(2\pi)^2} \int_{\Lambda - 2b}^{\Lambda} dk_{0x} \int_0^{\infty} k_{\perp} dk_{\perp} \frac{(k_{0x} + b) N_c^{\max}(t)}{\left[k_{\perp}^2 + (k_{0x} + b)^2\right]^{3/2}}$$
(S6.3)

$$= \frac{b}{\pi^2} E_z(t) N_c^{\text{max}}(t) \to 0.$$
 (S6.4)

In the final step we have considered the limit $\Lambda \to \infty$. The same reasoning applies to the first three terms in Eq. (22) of Ref. [2], demonstrating that the anomalous higher-order harmonics vanish in the limit $\Lambda \to \infty$ for the decoupled Weyl Hamiltonian.

Regarding Ref. [2], let us conclude with a comment on the significance of the separation between Weyl nodes and nonlinearities in the spectrum concerning the generation of anomalous higher-order harmonics. As established above, in the decoupled Weyl Hamiltonian, the anomalous higher-order response remains invariant, i.e. zero, under the separation between Weyl nodes. However, the introduction of nonlinearities leads to a finite anomalous higher-order response. Thus, in this simplified depiction, the importance of deviations from strict linearity for AHHG becomes clear.

S7. Normal harmonics

In Fig. S8 we show the results for normal harmonics for different values of γ , corresponding to Fig. 3 in the main text.

S8. Mirror symmetry

In this section, we introduce the notation $\mathbf{v}_{\perp} = (-v_x, v_y, v_z)$, where \mathbf{v} represents an arbitrary 3D vector. The Hamiltonian in the paper exhibits mirror symmetry: $H(\mathbf{k}) = H(\mathbf{k}_{\perp})$. From this symmetry, we deduce:

$$\mathbf{J}(\mathbf{k}_{\perp}, \mathbf{E}_{\perp}) = \mathbf{J}(\mathbf{k}, \mathbf{E})_{\perp}. \tag{S8.1}$$

Consider the polarization in the z direction. Then, $\mathbf{E}_{\perp} = \mathbf{E}$ holds, leading to:

$$J_x = \sum_{\mathbf{k}} J_x(\mathbf{k}, \mathbf{E}) = \sum_{k_x > 0} \left(J_x(\mathbf{k}, \mathbf{E}) + J_x(\mathbf{k}_\perp, \mathbf{E}) \right) = 0, \tag{S8.2}$$

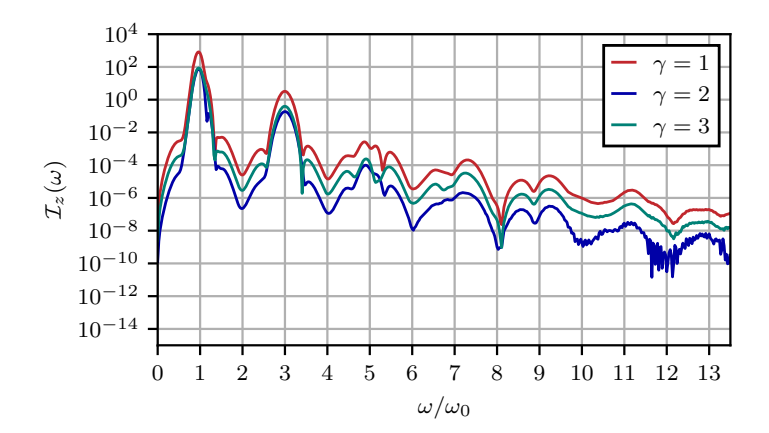


Figure S8. Normal spectrum \mathcal{I}_z for $\gamma = 1$, 2 and 3 (corresponding to 3 semi-Dirac nodes, 1 pair of Weyl nodes, and 1 semi-Dirac node, respectively).

i.e. there is no response in the direction of the Weyl node separation vector when the polarization of the laser is perpendicular to it.

^{*} luka.medic@ijs.si

^[1] H. K. Avetissian, A. K. Avetissian, G. F. Mkrtchian, and K. V. Sedrakian, Phys. Rev. B 85, 115443 (2012).

^[2] H. K. Avetissian, V. N. Avetisyan, B. R. Avchyan, and G. F. Mkrtchian, Phys. Rev. A 106, 033107 (2022).

^[3] Z.-Y. Li, Q. Li, and Z. Li, Chinese Physics B **31**, 124204 (2022).